

Capillary Forces between Sediment Particles and an Air–Water Interface

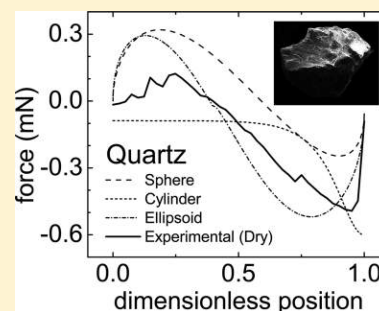
Nirmalya Chatterjee,^{*,†} Sergey Lapin,[‡] and Markus Flury[†]

[†]Department of Crop and Soil Sciences, Washington State University, Puyallup, Washington 98371, United States

[‡]Department of Mathematics, Washington State University, Pullman, Washington 99164, United States

S Supporting Information

ABSTRACT: In the vadose zone, air–water interfaces play an important role in particle fate and transport, as particles can attach to the air–water interfaces by action of capillary forces. This attachment can either retard or enhance the movement of particles, depending on whether the air–water interfaces are stationary or mobile. Here we use three standard PTFE particles (sphere, circular cylinder, and tent) and seven natural mineral particles (basalt, granite, hematite, magnetite, mica, milky quartz, and clear quartz) to quantify the capillary forces between an air–water interface and the different particles. Capillary forces were determined experimentally using tensiometry, and theoretically assuming volume-equivalent spherical, ellipsoidal, and circular cylinder shapes. We experimentally distinguished between the maximum capillary force and the snap-off force when the air–water interface detaches from the particle. Theoretical and experimental values of capillary forces were of similar order of magnitude. The sphere gave the smallest theoretical capillary force, and the circular cylinder had the largest force due to pinning of the air–water interface. Pinning was less pronounced for natural particles when compared to the circular cylinder. Ellipsoids gave the best agreement with measured forces, suggesting that this shape can provide a reasonable estimation of capillary forces for many natural particles.



1. INTRODUCTION

Soil particles in the colloidal fraction are relevant for their role in facilitation of subsurface contaminant transport.^{1,2} In unsaturated porous media, such as vadose zone sediments, the presence of the air–water interface plays an important role on fate and transport of colloids. Colloids can attach to stationary air–water interfaces in porous media.^{3,4} It has been observed that colloids can be mobilized during infiltration^{5–8} and drainage^{9,10} events. Sharma et al.¹¹ demonstrated that colloids attach and move along with air–water interfaces such as an infiltration front through a porous medium. Mechanistic studies involving pore-scale visualization confirm that colloids can be captured at the air–water interface and carried along with the moving air–water interface.^{12–17}

When a particle is attached to an air–water interface the particle experiences forces both due to surface tension and pressure differences. In a porous medium, these forces can cause a strong attraction of a particle to the stationary solid surfaces when the water saturation is low, and air–water interfaces pin the particles to solid surfaces.^{8,18,19} As water saturation increases and liquid films become thicker, this particle pinning disappears,^{19,20} and particles are even subject to a repulsive force that can lead to particle detachment from the solid surface.^{8,21} Theoretical calculations confirm that capillary forces can exceed DLVO forces.^{8,17,22,23}

Macroscopic techniques like tensiometry have been used to directly measure the capillary forces between a spherical particle and the air–water interface.^{24,25} More recently, microscopic

techniques like atomic force microscopy have been used to measure capillary forces for colloidal sized-particles.^{22,26–29} In these experiments, the measurements are usually done with spherical particles. Sphere tensiometry (i.e., using a sphere for tensiometric force measurements) has even been proposed as an alternative method to the de Noüy ring and Wilhelmy plate methods for measuring surface tensions and contact angles.^{30,31}

Capillary forces acting on a spherical particle can be calculated from theory using numerical solutions of the Young–Laplace equation.^{24,25,32,33} For particles with non-spherical but regular shapes, especially those with sharp edges the numerical solution becomes more complicated due to additional boundary conditions that need to be applied.^{34,35} The shape and surface properties of the particle determine the orientation of the air–water interface meniscus. The scale and degree of the roughness affects the magnitude of the capillary force and also determines how the interface moves across the solid surface, i.e., whether the interface slips or jumps, and where it jumps. No-slip conditions arise due to surface roughness conditions, where the air–water interface is temporarily being pinned.^{34,35}

In previous experiments,²¹ our group has quantified capillary forces on regularly shaped particles (spheres, cylinders, cubes)

Received: November 1, 2011

Revised: March 6, 2012

Accepted: March 19, 2012

Published: March 19, 2012

using tensiometry, and we have also made some force measurements on natural subsurface particles. Here, we expand upon those previous measurements, by focusing on natural subsurface particles and by quantifying the effects of particle shape and roughness. We further investigate the effect of natural surface coatings on the magnitude of the capillary force.

2. THEORY

Forces on a Particle in Contact with an Air–Water Interface. Figure 1 shows a schematic of an ellipsoidal and an

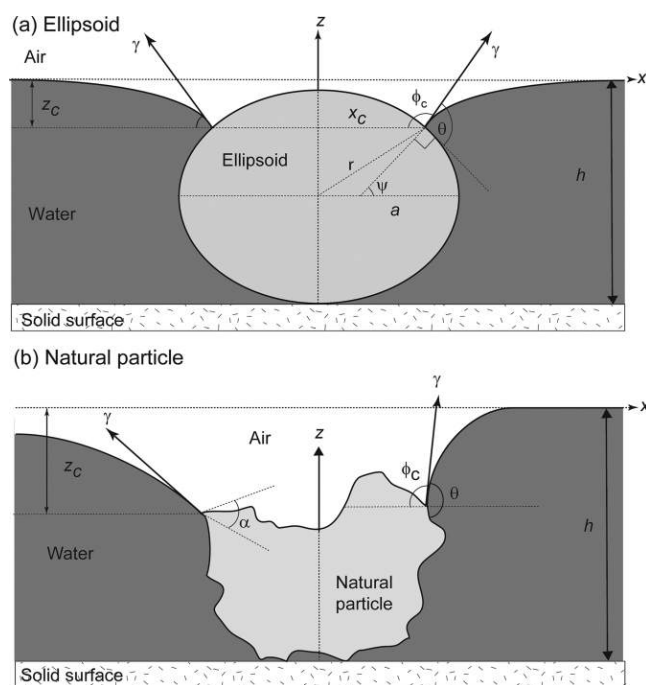


Figure 1. Forces acting (a) on a smooth, ellipsoidal particle with semiprincipal radii a , b , c , and (b) on an asymmetric, rough particle in contact with an air–water interface, where $\psi = (3\pi/2 - \theta - \phi_c)$ and α is the wedge angle for a sharp point on a surface where pinning occurs (see eq 3). Note that the interface line along the particle is undulating.

irregularly shaped particle attached to a solid surface and in contact with an air–water interface. The theory presented here follows the discussion presented in Zhang et al.²⁴ We consider that the solid surface is horizontal and that the air–water interface at $x \rightarrow \infty$ is also horizontal. The forces acting on the particle in a static system are (1) the DLVO force (f_{DLVO}), the (2) the gravity force (f_w), the (3) surface tension force (f_s), the (4) buoyancy force (f_b), and the (5) hydrostatic pressure force (f_p). The force balance on the particle is then given as²¹

$$f = f_{\text{DLVO}} + f_w + f_s + f_b + f_p \quad (1)$$

The sum of the surface tension (f_s) and hydrostatic pressure (f_p) forces is also known as the capillary force. If the particle is symmetric, the force balance f is parallel to the z -direction (Figure 1a), but if the particle is asymmetric (Figure 1b), the directions of f_s and f_p forces are determined by the contact angle of the air–water interface at the particle surface. Further, for asymmetric particles, the interface line is undulating in quadrupolar fashion.^{36–41} If $f < 0$ the particle will be detached from the solid surface, if $f > 0$ the particle will remain pinned to the solid surface.

Forces on an Ellipsoidal Particle at an Air–Water Interface. Here, we extend the theory for a spherical particle to a triaxial ellipsoid. Theoretical calculations^{36–43} of capillary forces on ellipsoidal particles showed that the contact line is of an undulating, elliptic shape rather than a flat ellipse. We calculated the length of the undulating contact line following the approach of van Nierop et al.⁴⁰ (see Supporting Information for details). The force balance on an ellipsoidal particle is then given as

$$f = 4\kappa E(e_{xy})\gamma \cos \beta \sin \phi_c + \pi ab \Delta \rho g z_c \cos^2 \beta - \frac{\pi}{3} \Delta \rho g abc (2 + 3 \sin \beta - \sin^3 \beta) \quad (2)$$

where a , b , and c are the semiprincipal axes of the ellipsoid along the three coordinate axes x , y , and z , respectively, κ is the ratio representing increase in contact line due to undulation, $E(e_{xy})$ is the complete elliptic integral of the second kind with eccentricity e_{xy} , β is the parametric latitude (Figure S.1, Supporting Information), γ is the surface tension of water, ϕ_c is the angle of inclination of the undistorted air–water interface at the three-phase contact line, $\Delta \rho = (\rho_l - \rho_g)$ is the difference between the two fluid densities ρ_l (water) and ρ_g (air), g is the acceleration due to gravity, and z_c is the deflection depth (position of the average contact line on the z -axis).

Forces on a Irregularly-Shaped Particle at an Air–Water Interface. The movement of the air–water interface (the macroscopic interface) on a solid surface is dependent on the geometry and the surface properties of the solid surface. In the case of ideally smooth surfaces, the air–water interface intersects the solid surface at an angle and a position determined by the capillary forces and the equilibrium air–water–solid contact angle.

In a dynamic system, where the air–water interface moves over a particle, surface roughness can cause the air–water interface to be pinned at surface discontinuities. While for a smooth particle, the air–water–solid interface line adjusts its position to the respective equilibrium position (Figure 1a), the pinning at surface discontinuities for rough particles causes the air–water interface to exceed its equilibrium configuration (Figure 1b). The increase in the contact angle can mathematically be formulated by the Gibbs extension of the Young equation:³⁵

$$\theta_0 < \theta < 180^\circ - \alpha + \theta_0 \quad (3)$$

where α is the wedge angle and θ_0 is the equilibrium contact angle for the vertical face (Figure 1b). The pinning causes the air–water interface to distort. These distortions cause large forces on the air–water interfaces, which tend to give way suddenly when the interface is moved beyond a critical distance, causing the contact line to snap off.

The approximation of a natural particle as a right, circular cylinder takes into consideration the maximum force due to the condition described by eq 3. The equation for the force balance on a right, circular cylinder²¹ is

$$f = -2\pi r \gamma \sin(\theta - \pi/2) - \Delta \rho g (z_0 + L) \pi r^2 \quad (4)$$

where L is the length of the cylinder.

Dimensionless Variables. The distances and forces can be represented in dimensionless form²⁴ as follows (capital letters represent dimensionless variables):

$$X = x\sqrt{c_a} \text{ and } Z = z\sqrt{c_a} \text{ and } R = r\sqrt{c_a} \text{ and } H = h\sqrt{c_a} \quad (5)$$

$$R_X = r_x\sqrt{c_a} \text{ and } R_Y = r_y\sqrt{c_a} \text{ and } R_Z = r_z\sqrt{c_a} \quad (6)$$

where x , y , and z are the directions parallel and perpendicular to the undisturbed air–water interface, r is the radius of the particle measured from the z -axis, h is the distance of the base of the particle from the undisturbed interface, and c is the capillary constant $c_a = \Delta\rho g/\gamma$, where $\Delta\rho$ is the density differences between the liquid and the gas, and γ is the surface tension. The dimensionless capillary force F is given as

$$F = \frac{f}{r^3 \Delta\rho g} \quad (7)$$

where f is the dimensional force.

3. MATERIALS AND METHODS

Particles. We used three particles of well-defined, standard shape and several natural sediment particles. The standard particles were made of PTFE and consisted of a sphere, a cylindrical disk, and a tent. The natural sediment particles came from the Hanford formation at the U.S. Nuclear Hanford Reservation in south-central Washington. The sediments were collected from 20 m depth below surface from a trench face at the Hanford Environmental Restoration Disposal Facility. The sediments were air-dried and sieved through meshes with nominal sizes 1 and 2 mm; the fraction between 1 and 2 mm was collected. We placed these sediments then under a dissection scope and picked individual particles with tweezers. We selected particles with typical mineralogy for the Hanford sediments: basalt, granite, hematite, magnetite, mica, milky quartz, and clear quartz. Three particles for each type of particle were selected and stored in 20 mL glass vials. Figure S.3 (Supporting Information) shows photographic images of the particles.

Individual sediment particles were mounted on J-shaped hooks made of steel wires with diameter of 0.5 mm (Figure S.4, Supporting Information). The lower end of the hooks was flattened with a file, and the hooks were cleaned by rinsing successively with acetone, ethanol, and deionized water. Particles were then attached to the hooks with instant glue (Dr. Bond SuperGlue, ITW Inc., Solon, Ohio). The lower end of the hook was attached to the bottom of the particle so that it did not interfere with the movement of the interface when it approaches the particle surface from the top. Particles were always handled with clean tweezers to avoid surface contamination.

Particle Characterization. Particles were characterized for air–water contact angles, shape, and surface roughness. The air–water–solid contact angle was determined using a goniometer (CA Goniometer Model 50–00–115, Ramé-Hart Instrument Co., Netcong, NJ). The PTFE particles and the natural particles as obtained were mounted on a microscopy slide using double-sided tape. A microsyringe (steel needle with 0.5 mm o.d.) was used to put a drop of water (25 μL) centered 0.3 mm away from the edge of the particle, so that the particle touched the side of the drop.

For electron microscopic characterizations, the particles were coated with platinum–palladium to a thickness of 3 nm under a sputter coater (Model 108auto, Cressington Scientific, Watford, England). The particles were then examined under an environmental scanning electron microscope (SEM) equipped with a field emission electron gun (FEI Quanta 200F, FEI Co., Hillsboro, OR). The particles were kept oriented under the SEM in the same manner as for the force-position and contact angle measurements. If observed directly from above, this gives the xy -plane view of the particle. Additional images were taken at a 90° view (xz -plane) to determine the overall cross-section of the particle. Particle dimensions were measured with the SEM measuring software. The SEM analysis was done after the contact angle and capillary force measurements (see below), because the surface properties were irreversibly altered by the sputter coating.

The particle outlines under the SEM in the xy - and xz -planes were used to determine the dimensions along the three coordinate axes. Figure 2 shows SEM images perpendicular to the xy -plane. We further calculated a root-mean-square value of the coordinates x , y , z , as well as a volume-equivalent spherical radius and ellipsoidal semimajor axes for each particle (see

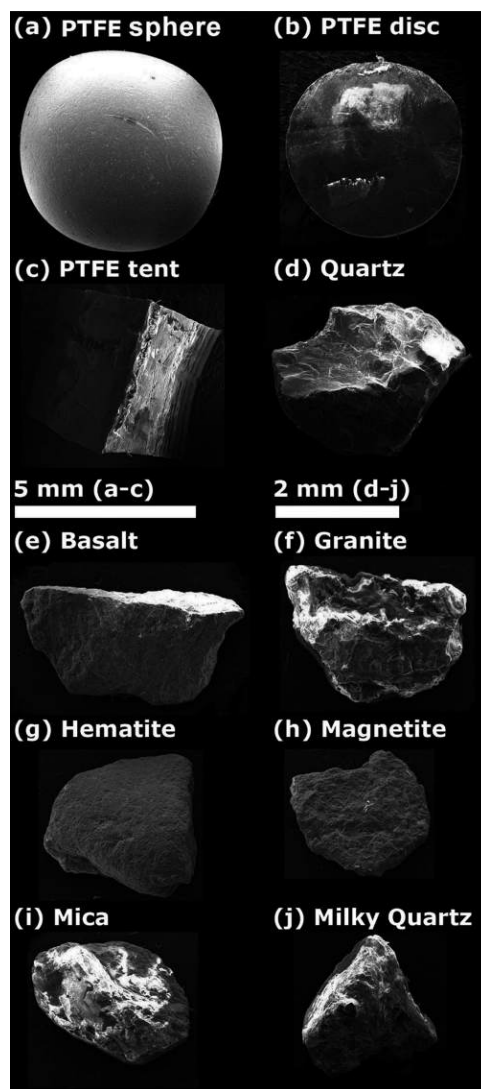


Figure 2. PTFE sphere, disk, and tent (a–c), and natural sediment particles (d–j) under field emission SEM, viewed perpendicular to the xy -plane.

Supporting Information for details on calculations and Tables S.1 and S.2 for summary of data).

Capillary Force Measurements. The capillary forces between the particles and the air–water interface were measured with a tensiometer (Process Tensiometer K100, Krüss GmbH, Hamburg, Germany). The precision of the tensiometer microbalance is 0.02 mg corresponding to a force of 0.196 μN . The J-shaped steel hook with the particle attached was fastened to the microbalance of the tensiometer (Figure S.4, Supporting Information). A glass cup (inner diameter 65.7 mm, height 37.9 mm) was filled with deionized water (electrical conductivity of 5.5 $\mu\text{S m}^{-1}$) and placed into the temperature jacket of the tensiometer (kept at 23 $^{\circ}\text{C}$).

The particle and the hook were initially in the air phase. The particle on the hook was kept stationary, while the air–water interface, formed in the glass cup below, was moved upward at a constant velocity of 1.0 mm min^{-1} , so that it approached the particle from the bottom (Figure S.4, Supporting Information). The interface made contact with the bottom part of the steel hook first, before wetting the particle itself. The tensiometer measured the force exerted on the microbalance after every position increment of 0.05 mm. These measurements were continued until the entire particle was completely immersed in water and the air–water interface had detached from the particle and passed to a position above the particle. The air–water interface was then lowered at the same velocity until the particle came back to its initial position above the interface in the air phase. By plotting force versus position, we obtained the so-called force-position curves.

Each particle was measured in a specific sequence of immersion and washing. First, the particle under air-dry conditions was mounted onto the tensiometer and immersed into the water to measure a force-position curve. This represents an initially dry particle, taken “as is” from the sediments, with its surface not modified by wetting or washing. Then, the particle was again immersed into the water, for five repeated cycles without allowing it to dry. These measurements represent force-position curves for an initially wet particle. After this sequence, the particle was washed with acetone and ethanol, and then air-dried for five minutes. The solvent rinsing was performed to remove soluble organic matter coatings on the particle surface. This cycle (one measurement for the air-dry particle and five for the wet particle) of immersion-emersion mentioned above was repeated with the cleaned particle. The data were then used to construct force-position curves for (1) dry, (2) wet, (3) cleaned-dry, and (4) cleaned-wet particles. The replicated runs for the wet (noncleaned and cleaned) particles were averaged and used to calculate error bars (standard deviations) for the force-position curves, and to determine the measurement precision.

For each particle, we used the same water in the glass cup, but we changed the water for every new particle. Surface tension of the water was measured before and after each force-position curve with the Wilhelmy plate method. The errors in force measurements are discussed in the Supporting Information.

4. DATA ANALYSIS

The force position curves were analyzed to determine the forces exerted on the particle by the moving air–water interface. We were particularly interested in the maximum detachment forces as well as the snap-off forces. The maximum detachment force is defined at the maximum force recorded by the tensiometer in

upward vertical direction, whereas the snap-off force is the force recorded when the air–water interface snaps off from the solid surface. The snap-off force was observed from the force–distance curve when the measured force decreased markedly within a short distance increment, which we found by computing the first derivative of the force–distance curve. The position where the change in force with change in position is maximal is the point of snap off.

We used the theory for a sphere (eq S.5, Supporting Information), a circular cylinder (eq 4), and a triaxial ellipsoid (eq 2) to calculate the forces acting on a particle in contact with the air–water interface as a function of the deflection depth z_c . The force plotted versus deflection depth gives the theoretical force-position curve.²⁴ We computed these theoretical curves for all particles (PTFE standard particles and natural sediment particles). To compute the forces for the natural particles, we approximated the particle shapes as spheres, cylinders, and ellipsoids, and used the measured shape parameters to calculate maximum and volume-equivalent radii and semimajor axes.

The theoretical calculations provide the maximum force; however, except for the cylindrical particle the snap-off force cannot be calculated because spheres and ellipsoids have no edges on which pinning can occur. A cylindrical particle should ideally have a snap-off force identical to the maximum force in the theoretical force-position curves.

5. RESULTS AND DISCUSSION

Interpretation of Force-Position Curves. Figure 3 shows an example of a force-position curve for a PTFE sphere. The solid line shows the measured capillary force experienced by the particle as the particle moved through the air–water interface. A zero force indicates that the particle does not experience any

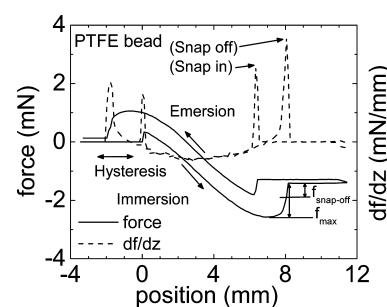


Figure 3. Example of a force-position curve for a PTFE sphere ($r = 2.78$ mm) showing the various segments of the curve during one immersion-emersion cycle and the differentiated force-position curve (dashed line).

net force due to the air–water interface. (The tensiometer balance is tared with the weight of the particle.) A positive force indicates that the particle is being pulled downward, that is, into the water phase, whereas a negative force indicates that the particle is pulled upward, that is, out of the water phase (compare Figure 1). The single-headed arrows along the plot show the direction of movement of the particle with respect to the air–water interface (immersion or emersion).

Initially, the particle is in the air-phase (net force is zero), when the particle contacts the air–water interface a downward capillary force (attractive capillary force) is recorded, indicated by the sudden occurrence of a net downward force. The magnitude of the net downward force at this position cannot be interpreted quantitatively because of the particle is attached to

the hook at the bottom; however, the snap-in can be detected unequivocally. This position of the air–water interface snap-in at the bottom of the particle is recorded for each particle and the z -value at this position is set to zero, that is, our reference position. During the immersion of the particle into the water phase, the force changes from positive to negative and reaches a minimum (or maximum negative force) at a distance of about 6.9 mm. This minimum corresponds to the maximum upward force experienced by the particle (including buoyancy). The air–water interface snaps off the particle just before the force recording becomes constant at a distance of about 8.2 mm. The constant force recorded after snap-off corresponds to the buoyancy. The maximum upward force (repulsive capillary force, f_{\max}) and the snap-off force ($f_{\text{snap-off}}$) are then determined by the difference between the recorded minimum force and the buoyancy force.

The emersion curve parallels the immersion curve, but is shifted because of hysteresis of the contact angle. The hysteresis of the contact angle not only affects the maximum forces exerted by the air–water interface, but also changes the position where the maximum forces and snap-off and snap-in occur.

The dashed curve in Figure 3 is the rate of change of the capillary force with respect to the change in position in the z -direction (df/dz) of the air–water interface. We use this curve to identify the exact position of the particle with respect to the interface where the maximum upward force ($df/dz = 0$) and the snap-off occur ($df/dz = \max$). In the following, we present the force-position curves in dimensionless form, so that different particles can be better compared with each other.

Theoretical Maximum Capillary Forces and Pressures.

Figure 4 shows theoretical force-position curves for the

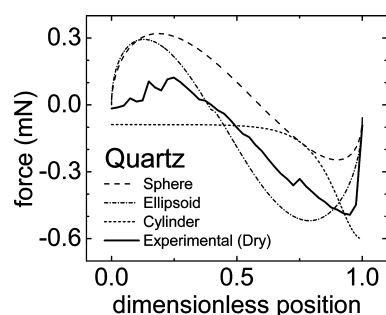


Figure 4. Force-position curves of sphere, circular cylinder, and ellipsoid (theoretical) and a dry, noncleaned quartz particle (experimental) during immersion. For the standard shapes, we used the calculated volume-equivalent dimensions (r_{ve}) of the quartz particle. [Dimensions of particles in mm are: sphere $r = 1.13$; ellipsoid $(a, b, c) = (1.47, 1.17, 0.83)$; cylinder $(r, h) = (1.47, 0.83)$; quartz $(x, y, z) = (1.54, 1.22, 0.81)$].

immersion of a sphere, an ellipsoid, and a circular cylinder compared with the measured curve for the quartz particle. For the theoretical curves, we assumed that the standard-shaped particles have the same volume as the quartz particle. The spherical particle shows the smallest forces during immersion, because it has the smallest circumference, and the cylinder shows the largest force, because the air–water interface is being pinned at the edges. The ellipsoid gives the closest approximation to the quartz particle in terms of the maximum capillary force.

Capillary forces can be translated to pressure by division by the particle cross-section. Capillary pressures associated with maximum forces were in the range of 100 Pa (Table S.3, Supporting Information). This indicates that, in porous media, the capillary forces on such millimeter-scale particles are important under fairly saturated conditions, for example during infiltration or imbibition.

Experimental Maximum and Snap-Off Capillary Forces.

Figure 5 shows the dimensionless force-position curves for the

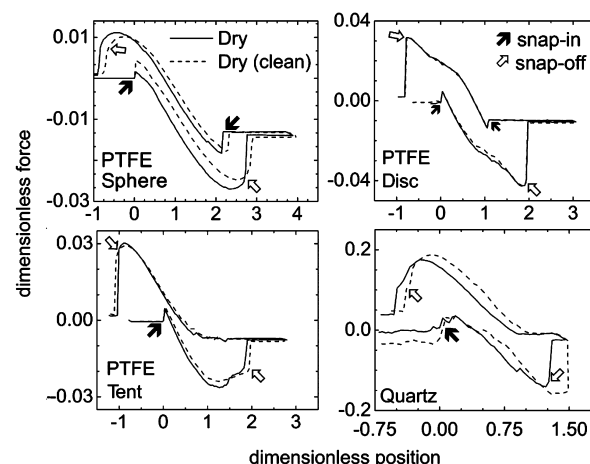


Figure 5. Experimental force-position curves of dry PTFE sphere, disk, and tent, and quartz (both cleaned and noncleaned). Filled arrows indicate snap-in, empty arrows indicate snap-off. Dimensions of particles are listed in Table S.1.

dry PTFE particles of standard shapes and for the quartz particle. We use quartz as example to illustrate the behavior of a natural sediment particle (results for the other sediment particles are shown in Figure S.6, Supporting Information). The shape of the curves for the standard particles are related to their geometries. The curves for the PTFE sphere and disk are symmetrical with the immersion and emersion curves almost exact mirror images. Both particles show a large snap-off force, with the disk showing the most pronounced snap-off effect due to interface pinning. The tent and the quartz particle also show snap-off force, due to interface pinning. However, during emersion, there was no snap-in for both the tent and the quartz particle, as the interacting surface area of the particle with the air–water interface is small.

The experimental force-position curves show that particles with a smooth surface show a more pronounced difference between maximum and snap-off forces. The PTFE sphere, with its smooth surface and minimal pinning of the air–water interface, shows a pronounced difference between maximum and snap-off force. The tent shows an even more pronounced difference between the two forces, because the snap-off force is small due the minimal interaction area of the tent tip with the air–water interface. A summary of all the experimental forces is given in Table S.4 (Supporting Information).

For the natural particles, the snap-off forces are, in general, smaller than the maximum capillary forces, but in some cases the snap-off force equals the maximum force. This occurs when the air–water interface is pinned at the particle surface strong enough so that snap-off happens under conditions represented by the Gibbs extension of the Young Equation (eq 3). The

more pronounced the pinning, the more likely the air–water interface snaps off at the maximum capillary force.

Effect of Solvent Cleaning. We expected that the solvent-cleaning would remove some organic coatings, and therefore, the cleaned particles would have a smaller contact angle than the noncleaned particles. This should manifest itself in smaller maximum upward and snap-off forces for the solvent-cleaned particles, but this was not observed in all cases. Basalt, milky quartz, hematite, and quartz showed larger forces for cleaned than for noncleaned particles (Tables S.4, Supporting Information). Closer examination of the force–distance curves shows that the snap-off forces for these four particles occurred at a greater z position for the clean particles compared to the noncleaned particles (Figure 5), suggesting that pinning was more pronounced for the clean particles. We infer that surface coatings may have covered and smoothed surface roughness, and that after solvent cleaning, more surface roughness was accessible to the air–water interface.

Figure 6 illustrates a complete measurement of force against position for the immersion of a quartz particle in the order they

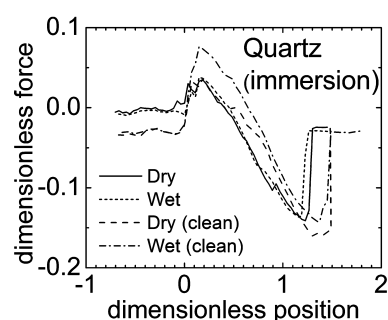


Figure 6. Force-position curves of a quartz particle during a sequence of immersion showing changes during the dry and wet stages (both cleaned and noncleaned).

were performed: first the immersion of the dry, noncleaned particle, then the wet, noncleaned particle, followed by the immersion of a cleaned and air-dried particle and last for the wet, cleaned particle. The initial, noncleaned dry particle showed large maximum and snap-off forces (solid line). After

wetting, the forces decreased, and snap off occurred earlier, indicated by the shift of the Z position to a smaller value. Similarly, the solvent-cleaned particle showed a left shift of the force–distance curve compared with the noncleaned particle. The solvent-cleaning also made the force–distance curve more symmetrical, indicating the cleaning reduced contact angle hysteresis.

Effect of Hysteresis. The immersion and emersion loops of the force–distance curves should, in the ideal case (i.e., in the absence of contact angle hysteresis and surface roughness), be symmetrical. The PTFE sphere indeed had a symmetrical curve, but the natural particles deviated from this symmetry, in some cases considerably (Figures 5 and S.6, Supporting Information). In general, the emersion curves were smoother than the immersion curves, which we attribute to the smaller contact angle during emersion (receding contact angle).

Comparison of Experimental and Theoretical Capillary Forces. Table 1 summarizes the experimental and calculated maximum capillary forces. The calculated forces are based on either the volume-equivalent or the maximum radius. The volume-equivalent radius tended to overestimate the measured radius, as shown for the PTFE sphere. For the sphere, the volume-equivalent radius was 14% higher than the measured radius. This led to a larger theoretical capillary force for the volume-equivalent radius than for the maximum radius. The theoretical calculations for the PTFE disk also overestimated the measured value. For the PTFE tent, using the volume-equivalent parameters provided close theoretical force values for both the sphere and the ellipsoidal shape. The theoretical calculations for a circular cylinder shape overestimated the force considerably, because the cylinder shape does not take into consideration the linearly reducing cross-section of the tent.

For the natural sediment particles, assuming a spherical shape (sphere) generally lead to an underestimation of the measured capillary force (Table 1). Assuming a circular cylinder, we overestimated the capillary force, whereas the ellipsoidal shape provided the best approximation of the capillary force.

6. IMPLICATIONS

Previous investigations have shown that capillary forces exerted at the air–water interface can exceed DLVO and gravity

Table 1. Maximum Capillary Forces (Experimental and Theoretical)

particle	capillary force (μN)								
	radius (mm)		experimental (dry, noncleaned)	theoretical					
				sphere		cylinder		ellipsoid ^b	
	r_{ve}^a	r_{max}^c		r_{ve}	r_{max}	r_{ve}	r_{max}	r_{ve}^d	r_{max}^e
PTFE sphere	3.17	2.79	−1305	−2150	−1652				
PTFE disk	2.09	2.40	−1292			−1510	−1961		
PTFE tent	2.25	2.99	−1204	−1096	−1903	−1718	−3000	−1446	−1565
basalt	1.15	1.78	−537	−221	−473	−1895	−1161	−738	−423
granite	1.17	1.46	−467	−297	−414	−998	−868	−479	−388
hematite	1.00	1.22	−279	−284	−374	−515	−676	−420	−396
magnetite	0.79	1.16	−422	−180	−298	−389	−637	−377	−432
mica	0.85	1.35	−526	−116	−246	−426	−769	−559	−506
milky quartz	1.07	1.01	−7	−396	−373	−560	−524	−479	−312
quartz	1.13	1.53	−402	−247	−403	−601	−936	−472	−543

^aVolume-equivalent spherical radius. ^bUndulating contact line. ^cMaximum of the three semimajor axes. ^dUses the maximum values of the three semimajor axes of the particle to scale the volume equivalent spherical radius to give a volume-equivalent ellipsoid equal in volume to the real particle. ^eUsing the maximum values of the three semimajor axes of the particle, does not give a volume-equivalent particle.

forces,^{8,21–23} and that moving air–water interfaces during infiltration can mobilize, i.e., detach, soil particles from stationary surfaces.^{11,12,17} In porous media, while under dry conditions, the capillary force is a strong attachment force of particles to stationary surfaces, under wet conditions, the capillary force becomes a mechanism of detachment of particles from stationary surfaces. Such wet conditions occur during infiltration or drainage. Here, we quantified, such as detaching capillary forces for differently shaped particles and found that measured capillary forces on natural particles can be approximated by a volume-equivalent ellipsoid. Thus, assuming an ellipsoidal shape allows us to better predict capillary forces experienced by natural particles in porous media. Capillary forces become more important the smaller the particles are, because the gravity force decreases faster with particle size than the capillary force, and the capillary pressure scales inversely with the particle radius. Thus, particularly for particles in the colloidal size range, the capillary forces will play a dominant role.

■ ASSOCIATED CONTENT

■ Supporting Information

Theoretical calculations of capillary forces on an ellipsoidal particle, data on measurement precision, and calculations of volume-equivalent dimensions, tables showing particle characterization data, experimental force measurements, and particle volume measurements, and figures showing dissection scope images of particles, experimental schematics, and force-position plots. This material is available free of charge via the Internet at <http://pubs.acs.org>.

■ AUTHOR INFORMATION

Corresponding Author

*Phone: +1-509-432-9533. E-mail: c_nirmalya@wsu.edu.

Notes

The authors declare no competing financial interest.

■ ACKNOWLEDGMENTS

This material is based upon work supported by the U.S. Department of Energy, Office of Science (BER), under Award No. DE-FG02-08ER64660.

■ REFERENCES

- (1) Kretschmar, R.; Borkovec, M.; Grolimund, D.; Elimelech, M. Mobile subsurface colloids and their role in contaminant transport. *Adv. Agron.* **1999**, *66*, 121–193.
- (2) McCarthy, J. F.; Zachara, J. M. Subsurface transport of contaminants. *Environ. Sci. Technol.* **1989**, *23*, 496–502.
- (3) Keller, A. A.; Auset, M. A review of visualization techniques of biocolloid transport processes at the pore scale under saturated and unsaturated conditions. *Adv. Water Resour.* **2007**, *30*, 1392–1407.
- (4) Wan, J. M.; Wilson, J. L.; Kieft, T. L. Influence of the gas–water interface on transport of microorganisms through unsaturated porous media. *Appl. Environ. Microbiol.* **1994**, *60*, 509–516.
- (5) Gao, B.; Sayers, J. E.; Ryan, J. N. Deposition and mobilization of clay colloids in unsaturated porous media. *Water Resour. Res.* **2004**, *40*, W08602 DOI: 10.1029/2004WR003189.
- (6) Jacobsen, O. H.; Moldrup, P.; de Jonge, H.; de Jonge, L. W. Mobilization and transport of natural colloids in a macroporous soil. *Phys. Chem. Earth.* **1998**, *23*, 159–162.
- (7) Levin, J. M.; Herman, J. S.; Hornberger, G. M.; Sayers, J. E. Colloid mobilization from a variably saturated, intact soil core. *Vadose Zone J.* **2006**, *5*, 564–569.
- (8) Shang, J.; Flury, M.; Chen, G.; Zhuang, J. Impact of flow rate, water content, and capillary forces on in situ colloid mobilization during infiltration in unsaturated sediments. *Water Resour. Res.* **2008**, *44*, W06411 DOI: 10.1029/2007WR006516.
- (9) Cheng, T.; Sayers, J. E. Mobilization and transport of in situ colloids during drainage and imbibition of partially saturated sediments. *Water Resour. Res.* **2009**, *45*, W08414 DOI: 10.1029/2008WR007494.
- (10) Zhuang, J.; McCarthy, J. F.; Tyner, J. S.; Perfect, E.; Flury, M. In-situ colloid mobilization in Hanford sediments under unsaturated transient flow conditions: Effect of irrigation pattern. *Environ. Sci. Technol.* **2007**, *41*, 3199–3204.
- (11) Sharma, P.; Abdou, H.; Flury, M. Effect of the lower boundary condition and flotation on colloid mobilization in unsaturated sandy sediments. *Vadose Zone J.* **2008**, *7*, 930–940.
- (12) Aramrak, S.; Flury, M.; Harsh, J. B. Detachment of deposited colloids by advancing and receding air–water interfaces. *Langmuir* **2011**, *27*, 9985–9993.
- (13) Gomez-Suarez, C.; Noordmans, J.; van der Mei, H. C.; Busscher, H. J. Removal of colloidal particles from quartz collector surfaces as simulated by the passage of liquid–air interfaces. *Langmuir* **1999**, *15*, 5123–5127.
- (14) Gomez-Suarez, C.; Noordmans, J.; van der Mei, H. C.; Busscher, H. J. Detachment of colloidal particles from collector surfaces with different electrostatic charge and hydrophobicity by attachment to air bubbles in a parallel plate flow chamber. *Phys. Chem. Chem. Phys.* **1999**, *1*, 4423–4427.
- (15) Leenaars, A. F. M.; O'Brien, S. B. G. Particle removal from silicon substrates using surface tension forces. *Philips J. Res.* **1989**, *44*, 183–209.
- (16) Noordmans, J.; Wit, P. J.; van der Mei, H. C.; Busscher, H. J. Detachment of polystyrene particles from collector surfaces by surface tension forces induced by air-bubble passage through a parallel plate flow chamber. *J. Adhesion Sci. Technol.* **1997**, *11*, 957–969.
- (17) Sharma, P.; Flury, M.; Zhou, J. Detachment of colloids from a solid surface by a moving air–water interface. *J. Colloid Interface Sci.* **2008**, *326*, 143–150.
- (18) Gao, B.; Steenhuis, T. S.; Zevi, Y.; Morales, V. L.; Nieber, J. L.; Richards, B. K.; McCarthy, J. F.; Parlange, J.-Y. Capillary retention of colloids in unsaturated porous media. *Water Resour. Res.* **2008**, *44*, W04504 DOI: 10.1029/2006WR005332.
- (19) Wan, J. M.; Tokunaga, T. K. Film straining of colloids in unsaturated porous media: Conceptual model and experimental testing. *Environ. Sci. Technol.* **1997**, *31*, 2413–2420.
- (20) Veerapaneni, S.; Wan, J.; Tokunaga, T. Motion of particles in film flow. *Environ. Sci. Technol.* **2000**, *34*, 2465–2471.
- (21) Shang, J.; Flury, M.; Deng, Y. Force measurements between particles and the air–water interface: Implications for particle mobilization in unsaturated porous media. *Water Resour. Res.* **2009**, *45*, W06420 DOI: 10.1029/2008WR007384.
- (22) Preuss, M.; Butt, H. J. Measuring the contact angle of individual colloidal particles. *J. Colloid Interface Sci.* **1998**, *208*, 468–477.
- (23) Scheludko, A.; Toshev, B. V.; Bojadjiev, D. T. Attachment of particles to a liquid surface (Capillary theory of flotation). *J. Chem. Soc., Faraday Trans. I* **1976**, *72*, 2815–2828.
- (24) Zhang, L.; Ren, L.; Hartland, S. More convenient and suitable methods for sphere tensiometry. *J. Colloid Interface Sci.* **1996**, *180*, 493–503.
- (25) Zhang, L.; Ren, L.; Hartland, S. Detailed analysis of determination of contact angle using sphere tensiometry. *J. Colloid Interface Sci.* **1997**, *192*, 306–318.
- (26) Preuss, M.; Butt, H. Direct measurement of particle-bubble interactions in aqueous electrolyte: dependence on surfactant. *Langmuir* **1998**, *14*, 3164–3174.
- (27) Gillies, G.; Kappl, M.; Butt, H. Direct measurements of particle–bubble interactions. *Adv. Colloid Interface Sci.* **2005**, *114*, 165–172.
- (28) Englert, A.; Krasowska, M.; Fornasiero, D.; Ralston, J.; Rubio, J. Interaction force between an air bubble and a hydrophilic spherical particle in water, measured by the colloid probe technique. *Int. J. Miner. Process.* **2009**, *92*, 121–127.

- (29) Yamamoto, T.; Harada, Y.; Fukui, K.; Yoshida, H. AFM investigation of the surface properties of silica particles dispersed by bead milling. *Colloids Surf. Physicochem. Eng. Aspects* **2010**, *362*, 97–101.
- (30) Gunde, R.; Hartland, S.; Mader, R. Sphere tensiometry: a new approach to simultaneous and independent determination of surface tension and contact angle. *J. Colloid Interface Sci.* **1995**, *176*, 17–30.
- (31) Ecke, S.; Preuss, M.; Butt, H. J. Microsphere tensiometry to measure advancing and receding contact angles on individual particles. *J. Adhesion Sci. Technol.* **1999**, *13*, 1181–1191.
- (32) Princen, H. M. Equilibrium shape of interfaces, drops, and bubbles. Rigid and deformable particles at interfaces. *Surface Colloid Sci.* **1969**, *2*, 1–84.
- (33) Zhang, P.; Johnson, W. P.; Rowland, R. Bacterial tracking using ferrographic separation. *Environ. Sci. Technol.* **1999**, *33*, 2456–2460.
- (34) Hesla, T. I.; Joseph, D. D. The maximum contact angle at the rim of a heavy floating disk. *J. Colloid Interface Sci.* **2004**, *279*, 186–191.
- (35) Singh, P.; Joseph, D. D. Fluid dynamics of floating particles. *J. Fluid Mech.* **2005**, *530*, 31–80.
- (36) Brown, A. B. D.; Smith, C. G.; Rennie, A. R. Fabricating colloidal particles with photolithography and their interactions at an air–water interface. *Phys. Rev. E* **2000**, *62*, 951–960.
- (37) Stamou, D.; Duschl, C.; Johannsmann, D. Long-range attraction between colloidal spheres at the air–water interface: The consequence of an irregular meniscus. *Phys. Rev. E* **2000**, *62*, 5263–5272.
- (38) Fournier, J.-B.; Galatola, P. Anisotropic capillary interactions and jamming of colloidal particles trapped at a liquid–fluid interface. *Phys. Rev. E* **2002**, *65*, DOI: 10.1103/PhysRevE.65.031601.
- (39) Danov, K. D.; Kralchevsky, P. A.; Naydenov, B. N.; Brenn, G. Interactions between particles with an undulated contact line at a fluid interface: Capillary multipoles of arbitrary order. *J. Colloid Interface Sci.* **2005**, *287*, 121–134.
- (40) van Nierop, E. A.; Stijnman, M. A.; Hilgenfeldt, S. Shape-induced capillary interactions of colloidal particles. *Europhys. Lett.* **2005**, *72*, 671–677.
- (41) Lehle, H.; Noruzifar, E.; Oettel, M. Ellipsoidal particles at fluid interfaces. *Eur. Phys. J. E* **2008**, *26*, 151–160.
- (42) Tee, G. J. *Surface Area and Capacity of Ellipsoids in n Dimensions*; Technical Report; Department of Mathematics, University of Auckland: Auckland, New Zealand, 2004.
- (43) Danov, K. D.; Kralchevsky, P. A. Capillary forces between particles at a liquid interface: General theoretical approach and interactions between capillary multipoles. *Adv. Colloid Interface Sci.* **2010**, *154*, 91–103.